A lightweight, ultrathin aramid-based flexible sensor using a combined inkjet printing and buckling strategy

Jianpeng Wu [a], Haoming Pang [a,*], Li Ding [b], Yu Wang [a], Xiaokang He [a], Quan Shu [a], Shouhu Xuan [a,*], Xinglong Gong [a,*]

[a] *CAS Key Laboratory of Mechanical Behavior and Design of Materials, Department of Modern Mechanics, CAS Center for Excellence in Complex System Mechanics, University of Science and Technology of China (USTC), Hefei 230027, China*
[b] *Shanghai Institute of Applied Mathematics and Mechanics, School of Mechanics and Engineering Science, Shanghai University, Shanghai 200444, China*

ARTICLE INFO

ABSTRACT

Flexible sensors toward lightweight and miniaturization are significant for easy monitoring. Herein, an ultrathin ($<$40 μm, 19 g m^{-2}) aramid-based flexible sensor is presented through expeditious inkjet printing and facile buckling strategy. Combining designable printing circuits with compressible buckled microstructures, the as-prepared sensor achieves excellent electrical response to external pressure without fussy preparation procedures and sophisticated facilities. The flexible sensor possesses sensitive subtle-pressure perception (38.4 Pa, 24 mg), remarkable mechanical durability (over 5500 cyclic compression and 4500 cyclic bending), as well as rapid response and recovery speed (20 ms). It can be conformably attached to skin/machine surfaces for continuous monitoring of physical signals originated from arterial pulses, human activities, and mechanical stimuli. As a digital printing process, conductive networks with different pixels are fully fabricated *via* inkjet printing to quantity pressure distribution. In addition, leveraging the hygroexpand-induced deformation of microstructures, the sensor can also discriminate the humidity-induced by multiple objects such as hand, cotton swab, and polyurethane sponge in a contactless fashion. Such a bimodal sensing system provides broad prospects for its applications in contact and noncontact perception platforms as a promising candidate for burgeoning portable electronic devices.

1. Introduction

With the development of modern manufacturing technologies, flexible sensing electronics have ignited tremendous attention in disease diagnosis, human–computer interface, as well as Internet of Things owing to their salient mechanical endurance, high sensitivity, and continuous monitoring [1–6]. Through mounting these electronics, devices/creatures are capable of perceiving multiple physical variations in external/internal environment, including pressure, strain, humidity, temperature, and magnetic field [7–11]. Prolific endeavors have been focused on designing high performance flexible sensors based on diverse transduction principles, such as resistive, capacitive, triboelectric, and electromagnetic modes [12–15]. Among them, resistive sensors are sought-after owing to their simple work process, rapid response, and micro-stimuli detection capability. For instance, introducing conductive component into soft polymers, high sensitive piezoresistive sensors can be easily prepared and applied in multiple fields [1,16,17]. Although the

existing resistive sensors have acquired prominent signal response to external stimuli, they inevitably sacrifice some valuable characteristics such as lightweight and miniaturization, which are urgently demanded in the next-generation portable electronic products.

Recently, an emerging printing electronics technology (*e.g.*, inkjet printing, screen printing, and gravure printing) has been adopted to effectively render flexible electronics with attributes of ultrathin and wearability [18]. By transferring electrical materials to planar supports, a variety of printing modules with scalable shapes and large-area circuits have been manufactured for supercapacitors, stretchable displays, energy-harvesting systems, and multifunctional passive components [19–22]. In particular, inkjet printing (IJP), a rapid mask-less manner, enabling controllable ink deposition on predefined trajectory as ubiquitous in daily office, possesses higher scalability and lower cost than screen printing and other manufacture methods [23]. Through the printing fashion, electrical units can be integrated onto thin substrates or films with minimal raw materials consumption, which allows sensing

---

electronics to elevate from conventionally bulky and rigid form factors to flexibility and miniaturization [23–25]. However, weak interaction between conductive constituents and dispersed phase usually causes ink aggregation and cartridge jam [26]. In addition, coffee rings and discontinuous pathways prefer to arise on printing substrates with poor wettability. Aramid nanofibers (ANFs) film, derived from Kevlar fabrics by sol–gel mean [27,28], can be processed into microscale thickness, which is thinner than general cellulose paper but keeps favorable wettability and superior mechanical strength. Inspired by previous vacuum filtration that embedded nanomaterials within ANFs film [29,30], it is expected to eliminate the above problems by developing the film into an ideal printing substrate for patterning circuits.

Although the insulation nature of ANFs film can be offset by printing circuits, low stretchability limits its applications in resistive sensors. Generally, for sensors with hierarchical constructions, structural compressibility enables enhanced deformation under external stimuli and further dictates the electrical signal changes [31–33]. Motivated by coarse epidermis of humans, modifying core sensing layers with geometric microarchitectures has been extensively utilized to improve sensing qualities including sensitivity and work range. Such structures involve unidirectional patterns (wrinkles, micro-ridges) [34–36], two-dimensional arrays (pyramids, hemispheres) [37,38], as well as random arrangements (abrasive paper-like surfaces) [39], whose distributions and sizes can be programmed to achieve optimal sensing properties. As for ANFs film, a feasible solution lies in the buckled microstructures design *via* a prestrain-releasing process. Distinguishing from previous reports [40,41] in which buckled films must keep bonding with thick substrates for normal operation, the ANFs film can be readily peeled off from substrate and preserve the resulting microstructures. Such a simple buckling treatment can complement the shortcoming of ANFs film in poor stimuli-response by imparting it with structural compressibility.

In this study, a strategy combining inkjet printing and buckling was proposed to fabricate an ultrathin (<40 μm, 19 g m^{-2}) ANFs-based flexible sensing electronics (AFSE). Briefly, the sensor was patterned with CNTs (carbon nanotubes) circuits using a household printer and then engineered with sinusoidal microstructures. The conductivity of CNTs circuits to different printing cycles, effect of prestrain on structural morphology, as well as sensing performance over compression and bending were systematically discussed. Potential applications of AFSE in monitoring physiological status, human activities, and machine movements as wearable electronics were further investigated. The scalable circuits designed *via* IJP was assisted in full fabrication of sensing arrays for pressure distribution detection. Moreover, the role of swelling effect in humidity response was explored to develop the AFSE toward contactless perception, whose humidity discrimination to the approached objects including fingertip, opisthenar, palm, cotton swab, and polyurethane sponge, was also verified.

2. Experimental

2.1. Materials

Kevlar fabrics were purchased from Junantai Protection Technologies Co., Ltd. Multi-wall carbon nanotubes (CNTs, $>95\%$) and N-Methyl-2-pyrrolidone (NMP) were obtained from Aladdin Inc. Dimethyl sulfoxide (DMSO) and potassium hydroxide (KOH) were supplied by Sinopharm Chemical Reagent Co., Ltd. Pluronic F-127 were provided by Sigma-Aldrich Inc.

2.2. Preparation of ANFs film

ANFs dispersion was synthesized from Kevlar fabrics by deprotonation with KOH according to earlier report [27]. Briefly, Kevlar fabrics (10 g) and KOH (10 g) were dissolving into DMSO (500 mL), followed by stirring for two weeks until the color turned to dark red. ANFs dispersion was then deposited on a plate (polymethyl methacrylate) using blade coating. A certain distance of 400 μm between blade and plate was fixed to acquire uniform thickness. The plate was further immersed in DI water for gelation of ANFs. The formed ANFs film was carefully peeled from the plate, and then preserved in fresh deionized (DI) water.

2.3. Inkjet printing of CNTs ink on ANFs film

CNTs (800 mg) were added to DI water (100 mL) along with Pluronic F-127 (2 g) and NMP (2.5 g), where Pluronic and NMP acted as stabilizers to improve the dispersion of CNTs. The mixture was subjected to an ultrasonic process for 100 min, followed by centrifuging twice for 30 min at 3000 r·min^{-1}. The supernatant was extracted and dried in an oven at 80 ℃. After drying to one-third of original volume, the resulting CNTs ink was transferred to a cartridge and then printed on ANFs film using a household printer (HP Deskjet 1112). Specifically, ANFs film was attached to the surface of polyethylene terephthalate (PET) film and then printed with specific patterns.

### 2.4. Preparation of ANFs-based sensor (AFSE)

AFSE was composed of buckled AFCT (ANFs film printed with CNTs) film (top), adhesive layer (middle), and flat AFCT film (bottom). The buckled AFCT film was prepared *via* a prestrain-releasing process. In detail, a compliant substrate (natural rubber) was uniaxially prestretched to a certain strain (ε_{pre}), followed by bonding AFCT film to its surface *via* Van der Waals, then released the prestrain on substrate slowly, which induced AFCT film to compress and form buckles. A series of ε_{pre} of 0%, 10%, 20%, 30%, and 40% were applied here. Next, a pure ANFs film as adhesive layer was sandwiched between the buckled and flat AFCT films (Fig. 1e). The central area (2.5 mm × 2.5 mm) of adhesive layer was cut off so that CNTs circuits could keep in contact. Finally, each AFCT film was pasted with copper foil or conductive tape as electrodes.

2.5. Characterization

The surface and cross-section morphologies were characterized by scanning electron microscopy (SEM, Gemini 500, Carl Zeiss Jena, Germany). Fourier transform infrared spectra was performed on FTIR spectrometer (Nicolet 8700, Thermo Nicolet, USA). Raman spectra was tested by a laser Raman spectrometer (LabRamHR, Jobin Yvon, France) with an excitation wavelength of 514 nm. The profiles of buckled microstructures were observed by Stylus profiler (XP-1, AMBIOS Inc.). Ink adhesion test was carried out by repeatedly sticking and peeling a 3 M tape (Scotch 810) from AFCT film according to previous report [42]. Tensile properties of AFCT films were carried out on a mechanical equipment (ElectroForce 3220, TA Instruments) with a loading rate of 2 mm min^{-1}. Electrical properties were measured using ModuLab test system (Solartron Analytical, AMETEK Advanced Measurement Technology, Inc.) with a supplied voltage of 1 V. The humidity sensing performance was tested in a closed box at room temperature (25 ± 1 ℃), where relative humidity was adjusted by a humidifier and recorded by a hygrothermoscope. Except for humidity related tests, all experiments were conducted in ambient atmosphere.

2.6. Buckling and compression simulations

All simulations were implemented by static method using Abaqus/CAE 6.13. For buckling process, AFCT film and compliant substrate were considered as elastic material and incompressible Neo-Hookean material, respectively. Bonding between film and substrate was realized by tie constraint. For compression simulation, the elastic buckled AFCT film was assumed to be sandwiched between two rigid plates, and positive pressure was acted on the top plate. Friction interactions (friction coefficient, 0.21) were set among film and plates [43].
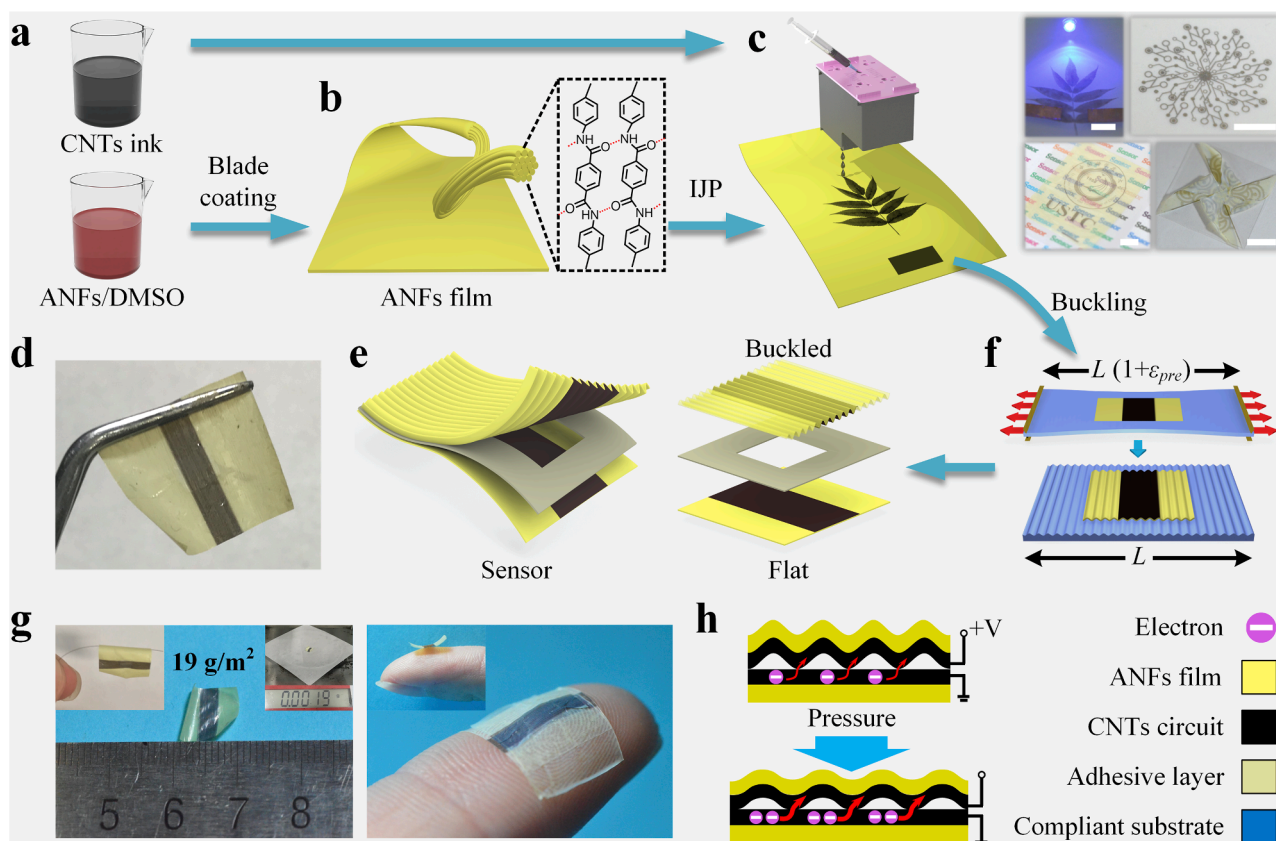
Fig. 1. Fabrication process and configuration of AFSE. (a) CNTs ink and ANFs/DMSO. (b) ANFs film prepared by blade coating. (c) Schematic diagram of IJP process and optical images of various printed patterns. Scale bars, 10 mm. (d) Photograph of prepared AFSE. (e) Assembling process and configuration of AFSE. (f) Schematic illustration of buckled microstructure by prestrain-releasing strategy. (g) Optical images of AFSE showing the characteristics of ultrathin, lightweight, and self-attachment. (h) Proposed sensing mechanism of AFSE. Note that all the AFSEs were made with prestrain of 40%.

3. Results and discussion

3.1. Fabrication and characterization of AFSE

Fig. 1a-d depicted the overall preparation procedure of AFSE, which mainly consisted of IJP, buckling, and assembling process. ANFs were split from Kevlar fabrics in DMSO/KOH, in which the nanofibers were dispersed homogeneously with a dark red color (Fig. 1a and Fig. S1a). The dispersion was then scraped on a plate and transferred into DI water to prepare ANFs film (Fig. 1b). The SEM images revealed that the as-formed film had a rugged surface and lamellar cross-section with a thickness of 5 ~ 7 μm (Fig. S2). Fig. 1c illustrated an expeditious IJP process, which was first utilized here to pattern circuits on ANFs film. The self-prepared CNTs ink (Fig. 1a and S1b, see *Experimental Section* for the fabrication method) was injected into a cartridge by syringe and printed on ANFs film surface with specific path. Sheet resistance of printed paths on ANFs film as the function of IJP cycles was depicted in Fig. S3. The conductivity was positively correlated with printing cycles and the sheet resistance decreased dramatically from 2 cycles of 21.5 MΩ to 4 cycles of 1.4 MΩ, implying the percolation threshold occurred at 3–4 cycles. To achieve optimal sensing performance and rational conductivity, 4 cycles were adopted in the subsequent fabrication of AFSE. As a digital printing process, various designed patterns including leaves, school badge, and circuits logo could be obtained (Fig. 1c and S4). The ANFs film printed with CNTs circuits (AFCT) could light up a blue light-emitting diode (LED) or be folded into the shape of a windmill, indicating its good conductivity and collapsible behavior. The AFCT film was further engineered with buckled microstructures through a typically prestrain-releasing treatment (Fig. 1f). Specifically, AFCT film was bonded to a pre-stretched elastomeric substrate by Van der Waals forces,

followed by releasing the substrate to its original length. The released prestrain (ε_{pre}) endowed AFCT film with periodic micro-waveforms, where ε_{pre} was determined by the length change of substrate before and after buckling.

Finally, the laminated AFSE was assembled with buckled AFCT (top), adhesive layer (middle), and flat AFCT (bottom), where pure ANFs film served as an adhesive layer was used to bond the upper and lower structures (Fig. 1d,e). Benefiting from the ultrathin and lightweight features of ANFs film, the prepared AFSE possessed a total thickness less than 40 μm (Fig. S5) as well as a surface density of 19 g m^{-2} (Fig. 1g), which could be easily held by a hair. It was also capable of conformally self-attaching to human skin as a wearable flexible electronics. Fig. 1h presented the schematic cross-section of AFSE, where the buckled and flat AFCT films were kept in contact in the initial state. A small amount of electrons flowed through the two CNTs layers, resulting in a weak conductivity. With pressure acted on the AFSE, the peaks of buckled microstructures were subjected to compression and tended to contact the lower layer more closely. The increased contact area gave more pathways for electrons to flow, leading to decreased resistance. In contrast to photolithography or laser etching, which suffered from complicated pre/post-treatment and mold fabrication [32], such buckling technology realized structural compressibility cost-effectively and expediently.

SEM (scanning electron microscopy) characterization was implemented as depicted in Fig. 2. The printed layer formed a clear boundary with ANFs film (Fig. 2a), in which CNTs were uniformly and densely deposited on the film surface with random orientation, thus leading to an entangled crosslink network for effective electron transmission (Fig. 2b,c). FTIR (Fourier transform infrared) and Raman spectra were utilized to observe the characteristic peaks of ANFs film, AFCT film, and
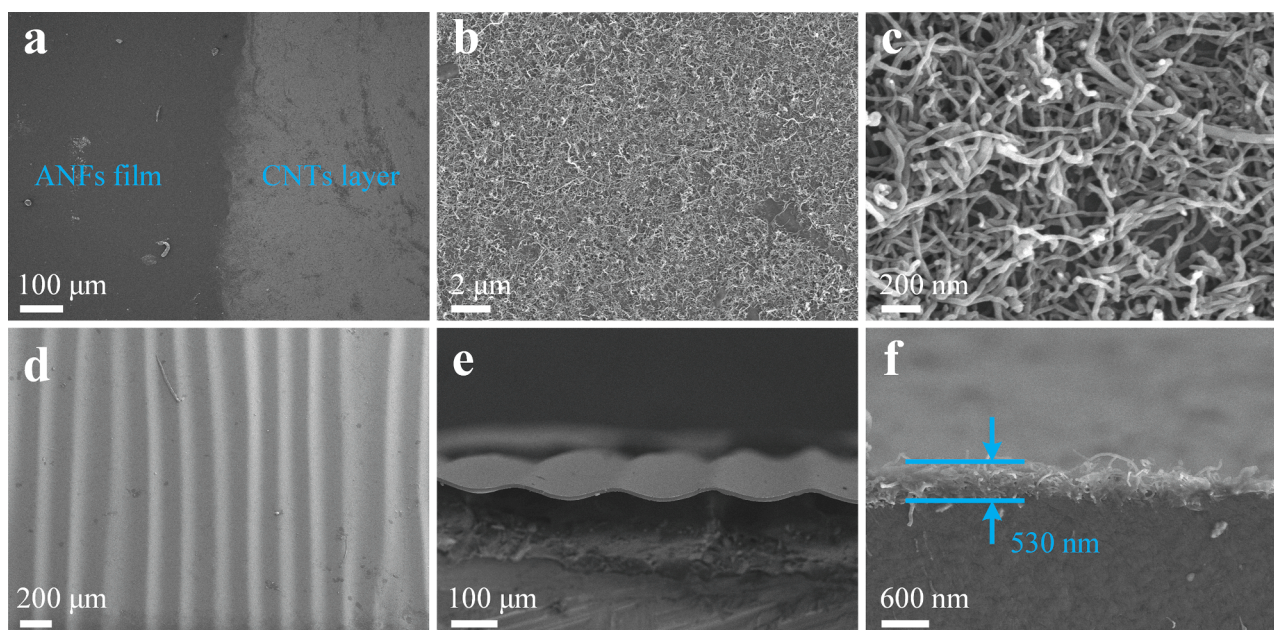
Fig. 2. SEM image characterization. (a) Surface of ANFs film with printed CNTs. (b-c) Magnified views of CNTs on the film surface. (d) Buckled microstructures of ANFs film. (e) Cross-section of the buckled morphology. (f) Cross-section of printed CNTs layer.

CNTs. The peaks at 3310 cm^{-1}, 1640 cm^{-1}, 1506 cm^{-1}, and 1015 cm^{-1} were respectively attributed to the vibrations of N–H stretch, C $=$ O stretch, C $=$ C stretch, and C–H bend (Fig. S6a) [27]. Raman spectra suggested the main peaks in ANFs were retained by AFCT film such as the C $=$ C vibration peaks of benzene rings [44], but the intensities were weaker compared to ANFs film due to the hindrance of coated CNTs layer during test (Fig. S6b). The SEM cross-section image revealed a CNTs layer entrapped on film surface with a negligible thickness (Fig. 2f, 530 nm), indicating that the conductive path could be realized with low ink-consumption *via* IJP. To evaluate the adhesion between CNTs layer

and ANFs film, peel-off test was performed on AFCT film using a 3 M tape (Fig. S7a). The relative resistance, $\Delta R/R_0$ ($\Delta R = R - R_0$, where R_0 and R represented the initial resistance and measured resistance under loading respectively), increased $\sim$ 40% after 10 repeats, reflecting a relatively strong durability of CNTs circuits. Furthermore, cyclic compression with 30 kPa was conducted on the film (Fig. S7b), only about 1% increment of $\Delta R/R_0$ was found which proved that the CNTs circuits still kept intact over high pressure. Obviously, this behavior was beneficial to subsequent pressure sensing. Fig. 2d,e validated the formation of buckled architecture with homogeneously periodic
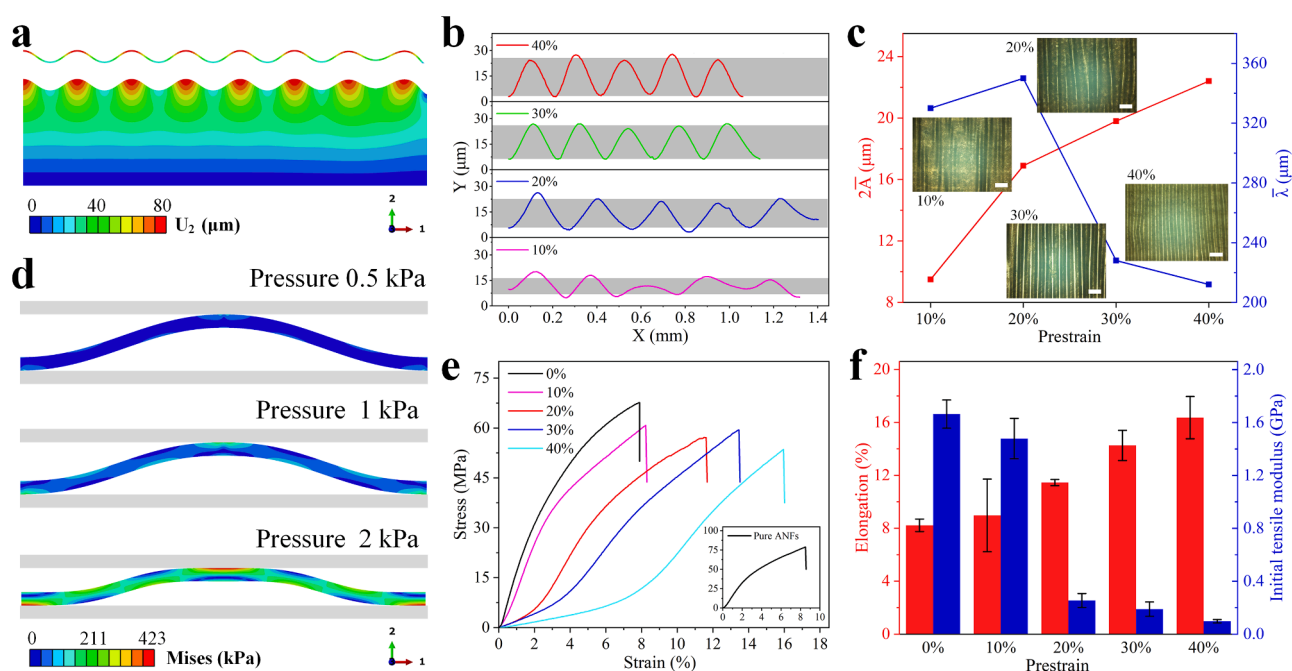
Fig. 3. Buckled microstructures analysis. (a) FEM of 2D half-model of film/substrate system. (b) Buckling contours of AFCT films with different ε_{pre} measured by a Stylus profiler. (c) The estimated values of wavelength and amplitude from (b) (The inset showed relevant microscope surface images. Scale bars, 400 μm). (d) FEM of a single wave compressed by two rigid plates. (e) Stress–strain curve of AFCT films with different ε_{pre}. (f) Initial tensile modulus and elongation of AFCT films with different ε_{pre}.

waveforms on AFCT film under 40% ε_{pre}, which would be further described in the next section.

3.2. Buckled microstructures analysis

Generally, buckling instability was susceptible to occur in stiff film/compliant substrate when compression was conducted on the system to reach a critical value [45–47]. Herein, exploiting a facile prestrain-releasing treatment, we functionalized the AFCT films with tunable sinusoidal micro-patterns by varying the released prestrain, ε_{pre}. FEM (Finite Element Method) presented a 2D half-model of film/substrate system, revealing a periodic wavy mode after the prestrain was completely released (Fig. 3a). Additionally, the buckled contours of the four AFCT films with ε_{pre} varying from 10% to 40% were further scanned by a Stylus profile and five cycles of each waveforms were displayed in Fig. 3b. The average values of wavelength ($\bar{\lambda}$) and double amplitude ($2\bar{A}$) with respect to ε_{pre} were extracted as shown in Fig. 3c. The minimum amplitude ($2\bar{A} = 9.5$ μm) occurred at $\varepsilon_{pre} = 10\%$ with irregular waveforms, whose corresponding microscope surface image (inset in Fig. 3c) manifested disorderly arrangement of microstructures, implying the onset of buckling instability at $\varepsilon_{pre} \approx 10\%$ in AFCT film. Further rise of ε_{pre} facilitated the evolution of waveforms toward well-defined structures as verified in the microscope images, accompanied by enhanced amplitude and shrunken wavelength. Here, the most obtrusive buckled microstructures were acquired at $\varepsilon_{pre} = 40\%$ ($\bar{\lambda} = 212$ μm, $2\bar{A} = 22.4$ μm). Ulteriorly, the tensile properties of AFCT films with different ε_{pre} were characterized by stress–strain curves (Fig. 3e). Compared to pure ANFs, the flat AFCT film showed a decreased elongation at break, which may be caused by stress concentration due to partly agglomerations of

printed CNTs. However, buckling treatment effectively promoted the stretchability of samples as ε_{pre} increased from 0% to 40%, and contributed to a 100% improvement of elongation from 8% to 16% (Fig. 3f). Meanwhile, the tensile modulus plummeted when ε_{pre} exceeded 10% owing to the transformation of film stretching to waveforms deformation at the initial loading phase (Fig. 3e,f). Fig. 3d showed the finite element model of a single wave based on the buckled AFCT film with 40% ε_{pre} that was compressed by two rigid plates. The peak structure collapsed progressively as the pressure grew from 0.5 kPa to 2 kPa, along with increased contact regime with rigid plates. The maximum local stress occurred at the contact center indicated a magnification effect to subtle external pressure [48], which was instrumental in subsequent sensing performance.

3.3. Sensing performance of AFSE

Fig. 4 showed the sensing properties of the final AFSE. During the test, AFSE was attached to the surface of an elastomeric substrate and compressed by a press tool with an area of 2.5×2.5 mm^2 (Fig. 4a). The sensitivity, $S = (\Delta R/R_0)/\Delta P$, where ΔP denoted as the change of external loading, was an essential factor to evaluate sensing performance. As mentioned above, the compressible buckled microstructures endowed device with increased contact area under compression. It allowed AFSE to perceive external pressure. To acquire the best sensing behavior, AFCT films with ε_{pre} varied from 0% to 40% were used to fabricate AFSEs, whose dependence of $-\Delta R/R_0$ on pressure was shown in Fig. 4b. The ε_{pre} of 0% represented flat structure without buckling, in which $-\Delta R/R_0$ rose slightly and linearly with pressure at the entire range of 0–8 kPa. The increased $-\Delta R/R_0$ was simply caused by the compacted interface between the upper and lower AFCT films under compression. No
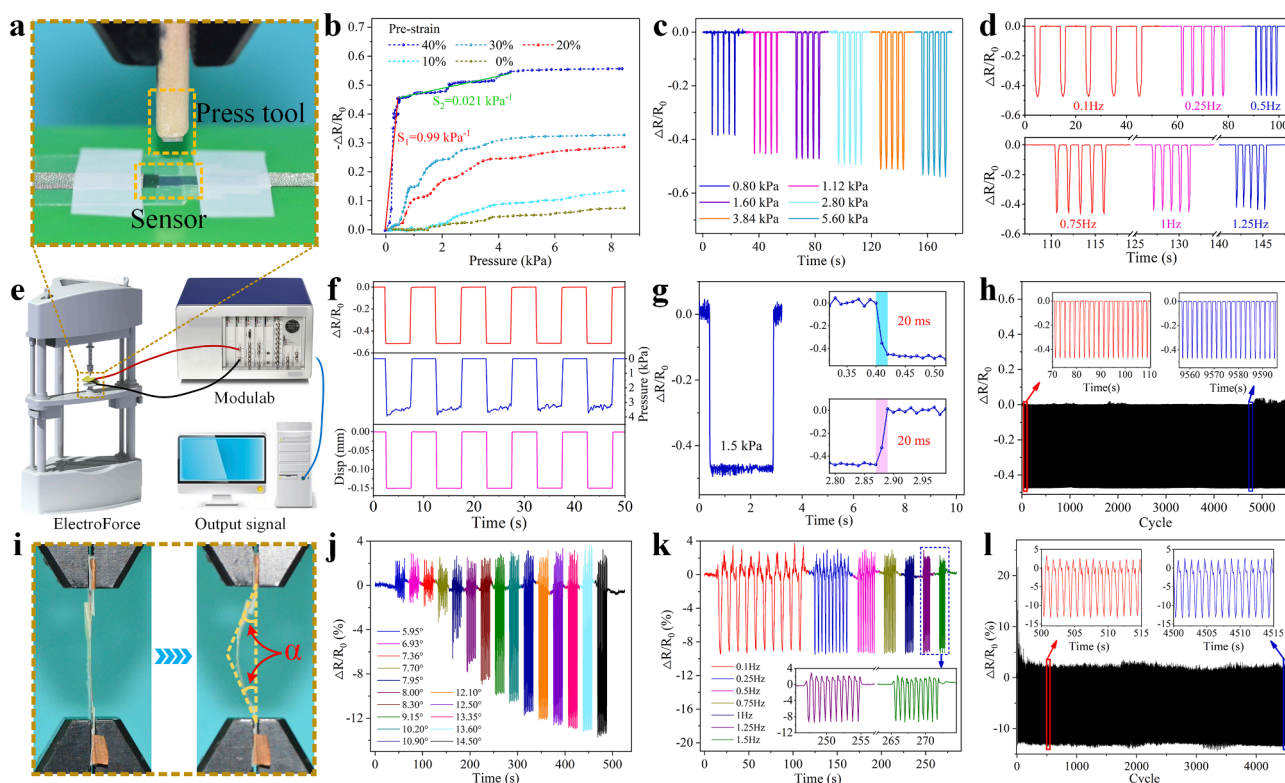
Fig. 4. Sensing characterization of AFSE over compression and bending. (a) Optical image of the compressive test system. (b) Sensitivity of AFSEs fabricated by buckled AFCT films with ε_{pre} varied from 0% to 40%. (c) Variation in $\Delta R/R_0$ toward different pressures. (d) Response of relative resistance to frequency at 0.1–1.25 Hz. (e) Schematic diagram of electric and force signal testing system. (f) Output signal of electric, pressure, and displacement under loading with periodic square waveforms. (g) Response time and recovery time at 1.5 kPa. (h) Compression stability performance at 0.5 Hz and 1.6 kPa. (i) Optical image illustrating the bending angle of AFSE. (j) Electrical response to different bending angles from 5.95° to 14.5°. (k) Change of $\Delta R/R_0$ with bending frequency at 0.1–1.5 Hz. (l) Cyclic bending test over 4500 cycles at 1 Hz. Note that the measured samples in (c)-(l) were made with $\varepsilon_{pre} = 40\%$.

obvious deformation happened during the process. When ε_{pre} grew to 10%, the buckled morphology was just formed with weak wave amplitude (Fig. 3a,b), contributing to limited deformation under loading. Therefore, the sensitivity to pressure was improved moderately compared to that of 0%. As ε_{pre} reached to 20% and 30%, the waveforms of buckled architecture were fully established (Fig. 3a), which allowed $-\Delta R/R_0$ to move up significantly during the compression process. However, the change of resistance was not obvious when pressure surpassed a critical value (3 kPa), reflecting that the contact area was saturated. It was noteworthy that the optimal sensing performance appeared at $\varepsilon_{pre} = 40\%$. Wherein, the $-\Delta R/R_0$ shot up remarkably below 0.6 kPa with a sensitivity of 0.99 kPa^{-1}, then slowed down to an extent of 0.021 kPa^{-1} at 0.6–4.42 kPa. The pressure resolution can be estimated approximately as ~ 68 Pa. Fig. S9 showed the variation in $\Delta R/R_0$ when loaded with specified compression displacement. The relative displacement ($\triangle D$) between adjacent points indicated a minimum displacement resolution of ~ 0.2 μm. Based on this result, buckled microstructures with $\varepsilon_{pre} = 40\%$ possessed distinguished piezoresistive effect, which was selected for followed testing.

Fig. 4c displayed the change of $\Delta R/R_0$ over different pressure. As pressure was tuned from 0.8 to 5.6 kPa, $-\Delta R/R_0$ of AFSE increased gradually, suggesting the related compression process conducted on buckled microstructures. Profiting from the stable buckled microstructures, AFSE presented a prominent frequency-independent feature. The variation degrees of $-\Delta R/R_0$ were almost identical over compression frequencies at 0.1–1.25 Hz (Fig. 4d). When loading with a cyclic square wave, the electric and displacement signals were consistent with external pressure (Fig. 4f), indicating that the AFSE could rapidly capture compression mode without delay. Furthermore, thanks to the elastic nature of ANFs film, the flexible sensor exhibited extremely swift respond/recovery time (20/20 ms, 90% of final value) under an instant loading and unloading of 1.5 kPa (Fig. 4g), where the total time of rising/falling edge was 60/20 ms. The quick response of AFSE was superior to most existing sensing devices and human skin [34,35,39,49], which guaranteed the capability to monitor external stimuli in real-time. Mechanically stability was an indispensable factor for piezoresistive sensors to withstand cyclic loading. Fig. 4h presented the repeated loading/unloading test at 1.6 kPa. The results indicated that no obvious attenuation or fluctuation of $\Delta R/R_0$ appeared even after 5500 cycles. The long-term fatigue test validated the marvelous durability of AFSE. Overall, such buckled microstructures endowed AFSE with favorable frequency-independence, rapid response speed as well as outstanding compression stability.

In addition, bend-sensing performance was also investigated. Specifically, AFSE was attached to a PET film, followed by compressing the film to induce bending, where the bending angle α was defined as the rotation angle from central axis of clamps (Fig. 4i). When α increased from 5.95° to 14.50° step by step in a manner of cyclic loading, the relative resistance of AFSE was declined correspondingly (Fig. 4j). The good response implied that bending process could lead to compression on buckled microstructures and then increased the contact area between CNTs layers. Moreover, $\Delta R/R_0$ exhibited more significant variations to α at the range of 5.95° to 8.30°, suggesting that AFSE was competent to monitor micro-bending motions with a limited value of 5.95°. Note that the initial positive change of $\Delta R/R_0$ (Fig. 4j) was probably caused by the tremor between electrodes and CNTs layers under each bending. Similar to compression process, the change of $\Delta R/R_0$ was irrespective of bending frequency at a broad range of 0.1–1.5 Hz (Fig. 4k). The robust adaptability ensured high-fidelity of output signal under different loading rates. Cyclic bending was further performed on AFSE. As shown in Fig. 4l, the buckled microstructures in AFSE were able to withstand over 4500 bending cycles without negligible fluctuation of $\Delta R/R_0$, which was fairly rare in recent researches. Therefore, the prepared ultrathin AFSE manifested exceptional sensing performance over compression and bending as an ideal candidate for future flexible wearable electronics.

3.4. Micro-tactile perception and sensor arrays design

The capability to perceive subtle pressure caused by mild motions or weights was eager to achieve on emerging electronic devices. As shown in Fig. 5a and Video S1, a tiny object (24 mg beads as shown in the inset of Fig. 5a) was gently placed on the surface of AFSE with a sensing area of 2.5×2.5 mm^2 and then picked up using a tweezer. A relevant variation in $\Delta R/R_0$ was appeared in this process, confirming the ability to detect tiny stimuli as low as 38.4 Pa (24 mg). The instant drop of signal in Fig. 5a induced by the tremor during loading/unloading also validated the rapid and sensitive response over dynamic force. Moreover, the ultrathin AFSE could be conformally adhered to the finger and connected with conductive tape to monitor a series of movements such as holding bead, pinching ball, and tapping keyboard (Fig. 5b). The output signals accurately distinguished the features between slight holding and quickly tapping. Therefore, incorporating the waveforms of buckled microstructures into ultrathin ANFs films, the prepared sensor exhibited outstanding micro-tactile sensing performance due to the enhanced structural compressibility. In addition, the designability of printed patterns *via* IJP technology rendered large-area fabrication of desirable circuit networks on ANFs films, which allowed AFSE to be used as multi-touch sensing. Herein, sensor arrays in 3×3 and 5×5 pixels were prepared respectively by designing specific conductive layouts. Fig. 5c showed the schematic configuration of the 3×3 array, in which both the flat and buckled AFCT films were printed with three parallel rectangle CNTs paths. The final size was 10×10 mm^2 with each pixel of 2.5×2.5 mm^2 (Fig. S10). When two small objects that weighted 57 mg and 161 mg (Fig. S11) were placed on the surface of 3×3 sensor array, the imposed pressures were quantitatively reflected on corresponding pixels with different signal responses (Fig. 5d). Similarly, the weight distributions at the center and four corners of a 3D printed plastic were also successfully mapped in the intensity profile as shown in Fig. 5e. What's more, a complete 5×5 circuit network (sensing area was 32×32 mm^2 with each unit of 4×4 mm^2) containing electrodes was fabricated *via* IJP process (Fig. 5f), followed by overlapping with a buckled AFCT film. A frog toy and an ant toy were arranged on specific position of this array, in which the applied pressures and contact sites were clearly recorded by the 2D mappings as presented in Fig. 5g. Overall, combining a controllable IJP approach with facile buckling treatment, the prepared sensor featured micro-tactile perception and multi-pixels sensing as a smart integrated circuit device in pressure monitoring.

3.5. Applications of AFSE in monitoring physiology and movements

Physiological signs such as arterial pulse and heartbeat were of significance to assess the health conditions of human bodies. For example, by analyzing the heart rate and pulse waveform, massive representative information like blood pressure, flow velocity, and aortic stiffness can be acquired for early health diagnosis [50]. Based on the property of micro-tactile perception, AFSE was further explored for monitoring body signals as a healthcare device. As shown in Fig. 6a, the detected pulse of wrist artery at normal state clearly reflected 10 cycles occurred in 8.5 s, with an estimated heart rate of ~ 70 beats per minute (bpm). The inset in Fig. 6a presented a single pulse process composed of percussion (P), tidal (T), and dicrotic (D) peaks. With these characteristic peaks, artery stiffness can be quantified using two typical parameters, namely augmentation index AIx= $(P-T)$ /PP (PP denoted as the pulse strength), and reflection index RIx = H /ΔT (H and ΔT represented the height of human being and time difference between P and D peaks respectively) [8,51,52]. For a 170 cm tall male, the calculated values of AIx and RIx were 37% and 3 m s^{-1} respectively, indicating a normal physiological level. After repeated deep squats for 5 min, the 10 pulses were completed in 6.5 s (heart rate of ~ 90 bpm) with notably improved intensity due to the dilated muscle arteries [3]. FFT (Fast Fourier Transform) analysis of waveform (right side of Fig. 6a) also showed the change of pulse in amplitude and frequency, confirming effective
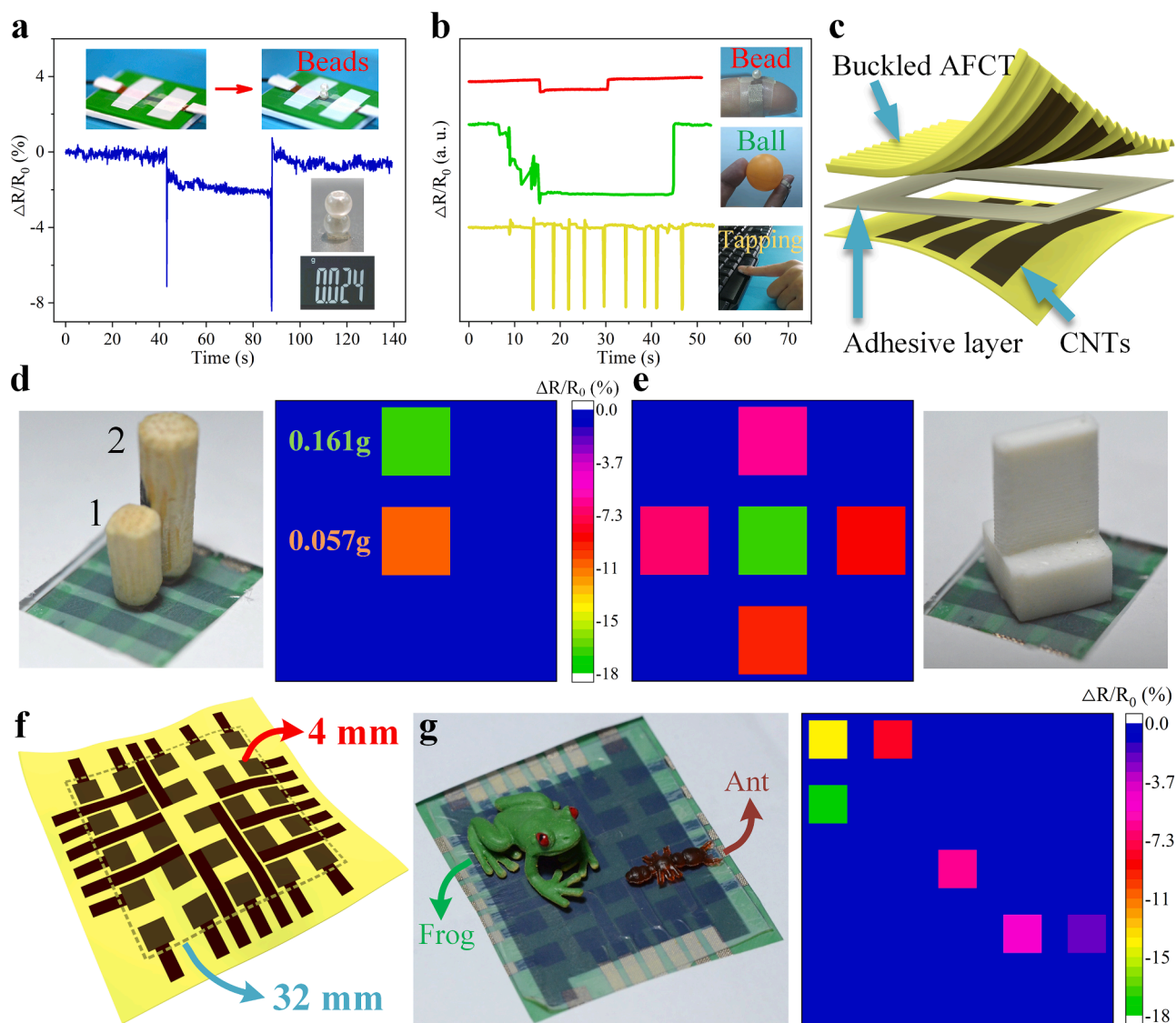
Fig. 5. Tactile sensing and applications of sensor arrays. (a) Response of $\Delta R/R_0$ to tiny beads that weighed 24 mg with relevant pressure of 38.4 Pa. The prepared sensor was attached to the surface of elastomeric substrate for measurement conveniently. (b) Detection of motions caused by holding bead, pinching ball, and tapping keyboard. (c) Schematics showing the configuration of 3 × 3 sensor array. (d, e) Optical images of 3 × 3 sensor array placed with different objects and the related 2D intensity profiles. (f) The bottom circuit network of 5 × 5 sensor array. (g) Photograph of a frog toy and an ant toy placed on the 5 × 5 sensor array and their pressure distribution mappings.

detectability of AFSE to physiology variations. Moreover, similar pulse waveforms at carotid and brachial arteries were recorded with corresponding rates of 66 and 77 bpm respectively (Fig. 6b), which were in good agreement with the wrist pulse. Even being fixed onto T-shirt, the AFSE could perceive every heartbeat near abdomen (Fig. S12).

Besides physiological markers, AFSE was capable of monitoring various physical activities such as blowing and respiration as depicted in Fig. 6c. Wherein, swift blowing action with gradually increased intensity was accurately captured by AFSE, and weak respiration cycles with a rate of 16 times min^{-1} also triged the resistance change, suggesting a remarkable micro airflow perception ability of AFSE. What's more, it could discriminate the cyclic wrist bending in different manners, i. e., reverting quickly and keeping bend state for ~ 8 s (Fig. 6e), which imparted reliability detection to multi-modal movements.

Owing to the flexible and ultrathin structure, AFSE could be conformally attached to a ruler to synchronously track the bend level during vibration process (Fig. 6g). As shown in Fig. 6f, the real-time response of $\Delta R/R_0$ reappeared a complete oscillation-attenuation behavior, in which the bending strength of ruler was progressively

weakened due to the inherent damping effect. The detected vibration frequency of ~ 20 Hz implied a prompt response capacity of AFSE to mechanical stimuli. Another real-time monitoring signal was collected from the joint bending induced by cyclic crawling of a spider robot, which constituted the repeated forward extension and backward retraction of legs (Fig. 6g and Fig. 6h). Analyzing the crawling period (0.7 s in pink region) and measured duration, we could infer that AFSE possessed superior continuous monitoring capability over 200 cycles. Overall, the prepared AFSE manifested broad application prospects in the health care and artificial intelligence platform.

3.6. Contactless perception

In addition, benefiting from the swelling effect of ANFs [53], buckled microstructures were able to deformation when underwent humidity stimuli and further lead to the alteration in electrical property of AFSE. To investigate the underlying humidity response capacity, the prepared sensor was placed in a closed environment (25 ± 1 °C) with controllable humidity. Fig. 7b illustrated the monitoring signal with increased
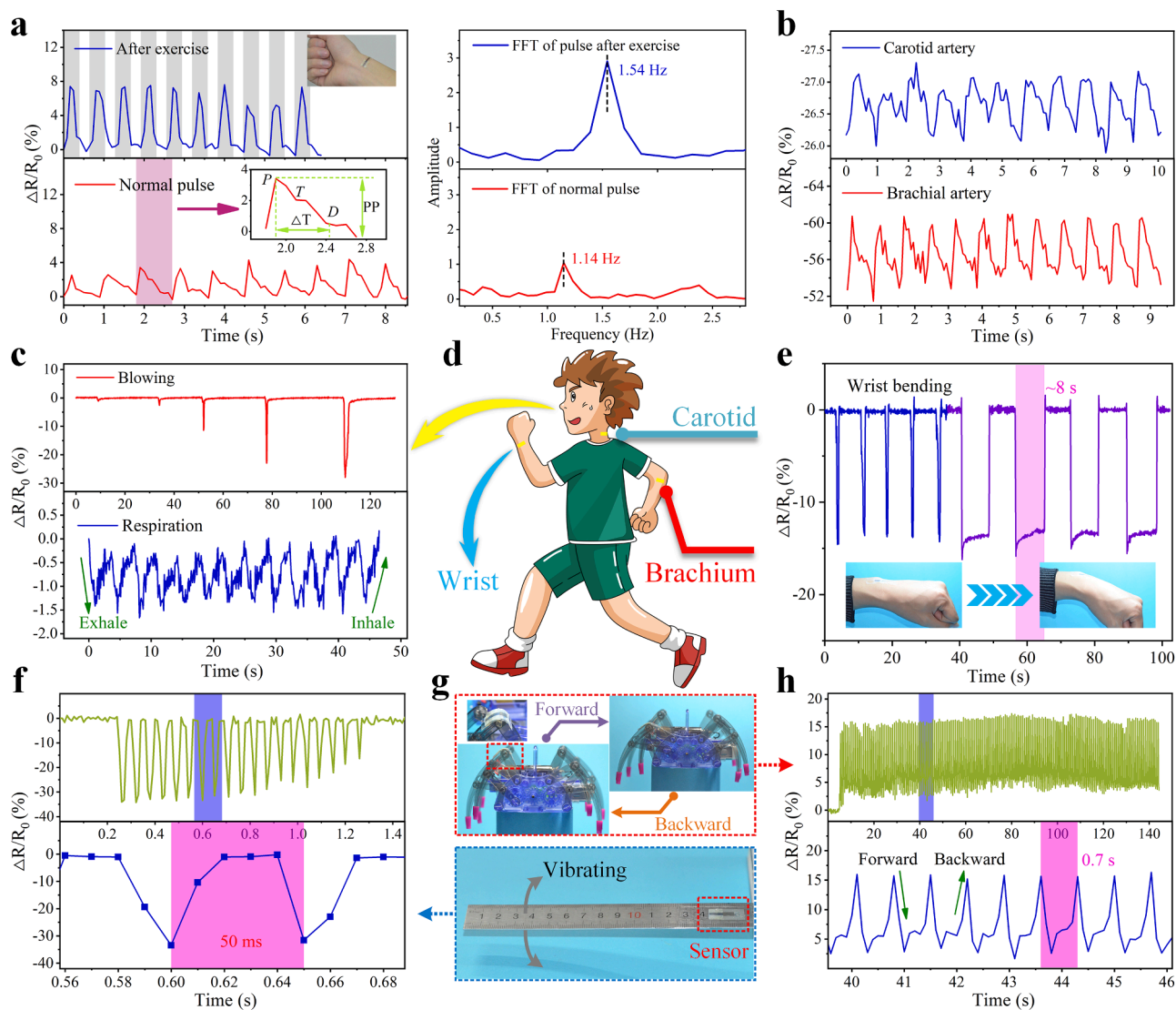
Fig. 6. Real-time monitoring of physiological signals and movements. (a) The detected wave and relevant FFT of wrist pulse under normal condition and after exercise (the inset showed single pulse waveform). (b) Pulse waveform recorded by AFSE attached on skin above carotid and brachial artery. (c) Real-time responses to airflow caused by blowing and respiration conducted on the surface of AFSE. (d) Schematic illustrating the applications of AFSE in body signal monitoring. (e) Detection of wrist bending with and without staying for a while. Detection of cyclic activities produced by (f) ruler oscillating and (h) crawling of a spider robot (the pink regions denoted as related motion periods). (g) Photograph of AFSEs pasted to spider foot and ruler respectively for measurement. (For interpretation of the references to color in this figure legend, the reader is referred to the web version of this article.)

relative humidity (RH), indicating a preeminent dependence at the region from 60% to 95%. Fig. 7c presented the electrical response to cyclic variation of RH between 50% and 80%. The slight fluctuation at corresponding RH suggested favorable stability and recoverability toward dynamic environment. Based on this result, AFSE had promising potential in noncontact perception (Fig. 7a), which avoided direct mechanical impairment to devices. For example, AFSE was capable of differentiating the moisture near fingertip at a series of vertical height from 0.5 mm to 4.5 mm (Fig. 7d) with approximatively linear signal change. Repeated fingertip approaching movements also could be realtimely detected (Fig. 7e). Moreover, it exhibited favorable humidity discrimination over multiple objects such as a fingertip, opisthenar, palm, wet cotton swab, and wet polyurethane (PU) sponge that were employed to approach the device in sequence (Fig. 7f). Among them, the peak 1 and 2 referred to the measured signals form opisthenar before and after daubing DI water, respectively, whose significant difference implied viable perception to humidity changes of skin. A similar experiment procedure was conducted at the condition of wearing glove and dry state (Fig. S13 and Video S2) for comparison, in which no

pronounced signal change was observed, confirming the purely humidity-driven response of AFSE. In a word, our ANFs-based flexible sensor exhibited outstanding overall performance, *e.g.* high sensitivity, swift response, low limit of detection, and humidity perception, compared with the existing resistive sensors (Table S1).

4. Conclusions

Harnessing expeditious IJP process and agile buckling treatment, an ANFs-based flexible sensing electronics (AFSE) with ultrathin morphology was successfully prepared that combined designable printed circuits with well-aligned buckled microstructures. Since the buckled micro-patterns-enabled structural compressibility, AFSE possessed exceptional piezoresistive sensing performance, including subtle pressure perception as low as 38.4 Pa (24 mg), swift response/recovery time (20 ms), as well as outstanding durability over compression (5500 cycles), and bending (4500 cycles), which provided feasible monitoring in physiological states, physical activities, and mechanical stimuli as a wearable device. Furthermore, scalable conductive networks
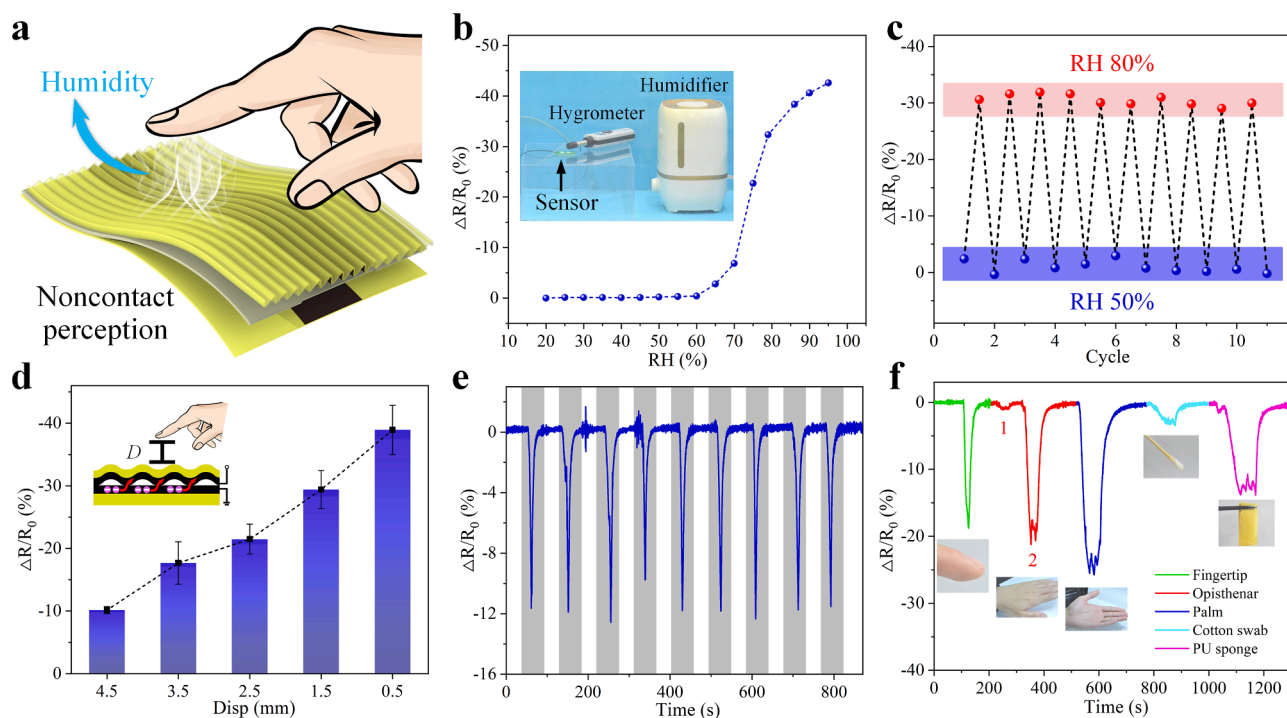
Fig. 7. Humidity sensing performance of AFSE. (a) Schematics illustrating humidity stimuli over AFSE. (b) The dependence of $\Delta R/R_0$ on RH (Inset showed humidity measurement setup). (c) Change of $\Delta R/R_0$ between 50% and 80% for 10 cycles. Electrical response to (d) fingertip approaching with different vertical displacement and (e) repeated fingertip approaching movements. (f) Electrical response to various moisture emitted from fingertip, opisthenar, palm, wet cotton swab, and wet PU sponge.

were fully fabricated *via* the controllable IJP process, allowing AFSE to quantity the pressure distribution of different objects. Inspiringly, it also exhibited excellent humidity response capability owing to the intrinsic hygroexpansive property of ANFs, being capable of detecting RH cyclic change between 50% and 80% as well as the moisture emitted from multiple objects such as fingertip, cotton swab, and PU sponge. Based on the dual-model response to pressure and humidity, the ultrathin flexible electronics manifested potential applications in health diagnosis, artificial intelligence systems, and noncontact control.

Declaration of Competing Interest

The authors declare that they have no known competing financial interests or personal relationships that could have appeared to influence the work reported in this paper.

Appendix A. Supplementary data

Supplementary data to this article can be found online at https://doi.org/10.1016/j.cej.2021.129830.

References

[1] Q.i. Wu, Y. Qiao, R. Guo, S. Naveed, T. Hirtz, X. Li, Y. Fu, Y. Wei, G.e. Deng, Y. i. Yang, X. Wu, T.-L. Ren, Triode-mimicking graphene pressure sensor with positive resistance variation for physiology and motion monitoring, ACS Nano 14 (8) (2020) 10104–10114, https://doi.org/10.1021/acsnano.0c0329410.1021/acsnano.0c03294.s001.

[2] M.J. Zhong, L.J. Zhang, X. Liu, Y.N. Zhou, M.Y. Zhang, Y.J. Wang, L. Yang, D. Wei, Wide linear range and highly sensitive flexible pressure sensor based on multistage sensing process for health monitoring and human-machine interfaces, Chem. Eng. J. 412 (2021) 128649, https://doi.org/10.1016/j.cej.2021.128649.

[3] M. Fu, J. Zhang, Y. Jin, Y. Zhao, S. Huang, C.F. Guo, A highly sensitive, reliable, and high-temperature-resistant flexible pressure sensor based on ceramic nanofibers, Adv. Sci. 7 (17) (2020) 2000258, https://doi.org/10.1002/advs.v7.1710.1002/advs.202000258.

[4] Z. Liu, K. Chen, A. Fernando, Y. Gao, G. Li, L.u. Jin, H. Zhai, Y. Yi, L. Xu, Y. Zheng, H. Li, Y. Fan, Y.i. Li, Z. Zheng, permeable graphited hemp fabrics-based, wearing-comfortable pressure sensors for monitoring human activities, Chem. Eng. J. 403 (2021) 126191, https://doi.org/10.1016/j.cej.2020.126191.

[5] J.-H. Lee, J. Kim, D. Liu, F. Guo, X.i. Shen, Q. Zheng, S. Jeon, J.-K. Kim, Highly aligned, anisotropic carbon nanofiber films for multidirectional strain sensors with exceptional selectivity, Adv. Funct. Mater. 29 (29) (2019) 1901623, https://doi.org/10.1002/adfm.v29.2910.1002/adfm.201901623.

[6] T. Ha, J. Tran, S. Liu, H. Jang, H. Jeong, R. Mitbander, H. Huh, Y. Qiu, J. Duong, R. L. Wang, P. Wang, A. Tandon, J. Sirohi, N. Lu, A chest-laminated ultrathin and stretchable e-tattoo for the measurement of electrocardiogram, seismocardiogram, and cardiac time intervals, Adv. Sci. 6 (14) (2019) 1900290, https://doi.org/10.1002/advs.v6.1410.1002/advs.201900290.

[7] N. Bai, L. Wang, Q.i. Wang, J. Deng, Y. Wang, P. Lu, J. Huang, G. Li, Y. Zhang, J. Yang, K. Xie, X. Zhao, C.F. Guo, Graded intrafillable architecture-based iontronic pressure sensor with ultra-broad-range high sensitivity, Nat. Commun. 11 (1) (2020), https://doi.org/10.1038/s41467-019-14054-9.

[8] B. Yin, Y. Wen, T. Hong, Z. Xie, G. Yuan, Q. Ji, H. Jia, Highly stretchable, ultrasensitive, and wearable strain sensors based on facilely prepared reduced graphene oxide woven fabrics in an ethanol flame, ACS Appl. Mater. Interfaces 9 (37) (2017) 32054–32064, https://doi.org/10.1021/acsami.7b0965210.1021/acsami.7b09652.s00110.1021/acsami.7b09652.s00210.1021/acsami.7b09652.s00310.1021/acsami.7b09652.s004.

[9] L. Xu, H. Zhai, X. Chen, Y. Liu, M. Wang, Z. Liu, M. Umar, C. Ji, Z. Chen, L.u. Jin, Z. Liu, Q. Song, P. Yue, Y.i. Li, T.T. Ye, Coolmax/graphene-oxide functionalized textile humidity sensor with ultrafast response for human activities monitoring, Chem. Eng. J. 412 (2021) 128639, https://doi.org/10.1016/j.cej.2021.128639.

[10] K. Song, R. Zhao, Z.L. Wang, Y.a. Yang, Conjuncted pyro-piezoelectric effect for self-powered simultaneous temperature and pressure sensing, Adv. Mater. 31 (36) (2019) 1902831, https://doi.org/10.1002/adma.v31.3610.1002/adma.201902831.

[11] L.i. Ding, S. Xuan, L. Pei, S. Wang, T. Hu, S. Zhang, X. Gong, Stress and magnetic field bimode detection sensors based on flexible CI/CNTs-PDMS sponges, ACS Appl. Mater. Interfaces 10 (36) (2018) 30774–30784, https://doi.org/10.1021/

acsami.8b1133310.1021/acsami.8b11333.s00110.1021/acsami.8b11333.
s00210.1021/acsami.8b11333.s003.

[12] L.i. Ding, Y.u. Wang, C. Sun, Q. Shu, T. Hu, S. Xuan, X. Gong, Three-dimensional structured dual-mode flexible sensors for highly sensitive tactile perception and noncontact sensing, ACS Appl. Mater. Interfaces 12 (18) (2020) 20955–20964, https://doi.org/10.1021/acsami.0c0399610.1021/acsami.0c03996.s001.

[13] Y. Park, J. Shim, S. Jeong, G.-R. Yi, H. Chae, J.W. Bae, S.O. Kim, C. Pang, Microtopography-guided conductive patterns of liquid-driven graphene nanoplatelet networks for stretchable and skin-conformal sensor array, Adv. Mater. 29 (21) (2017) 1606453, https://doi.org/10.1002/adma.201606453.

[14] S. Wang, L. Gong, Z. Shang, L.i. Ding, G. Yin, W. Jiang, X. Gong, S. Xuan, Novel safeguarding tactile e-skins for monitoring human motion based on SST/PDMS-AgNW-PET hybrid structures, Adv. Funct. Mater. 28 (18) (2018) 1707538, https://doi.org/10.1002/adfm.v28.1810.1002/adfm.201707538.

[15] H. Askari, Z. Saadatnia, E. Asadi, A. Khajepour, M.B. Khamesee, J. Zu, A flexible hybridized electromagnetic-triboelectric multi-purpose self-powered sensor, Nano Energy 45 (2018) 319–329, https://doi.org/10.1016/j.nanoen.2018.01.011.

[16] T. Hu, S. Xuan, L.i. Ding, X. Gong, Liquid metal circuit based magnetoresistive strain sensor with discriminating magnetic and mechanical sensitivity, Sens. Actuators B Chem. 314 (2020) 128095, https://doi.org/10.1016/j.snb.2020.128095.

[17] X.-F. Zhao, C.-Z. Hang, H.-L. Lu, K.e. Xu, H. Zhang, F. Yang, R.-G. Ma, J.-C. Wang, D.W. Zhang, A skin-like sensor for intelligent braille recognition, Nano Energy 68 (2020) 104346, https://doi.org/10.1016/j.nanoen.2019.104346.

[18] Y. Zhang, L. Zhang, K. Cui, S. Ge, X. Cheng, M. Yan, J. Yu, H. Liu, Flexible electronics based on micro/nanostructured paper, Adv. Mater. 30 (51) (2018) 1801588, https://doi.org/10.1002/adma.v30.5110.1002/adma.201801588.

[19] K.-H. Choi, JongTae Yoo, C.K. Lee, S.-Y. Lee, All-inkjet-printed, solid-state flexible supercapacitors on paper, Energ. Environ. Sci. 9 (9) (2016) 2812–2821, https://doi.org/10.1039/C6EE00966B.

[20] J. Kim, H.J. Shim, J. Yang, M.K. Choi, D.C. Kim, J. Kim, T. Hyeon, D.-H. Kim, Ultrathin quantum dot display integrated with wearable electronics, Adv. Mater. 29 (38) (2017) 1700217, https://doi.org/10.1002/adma.201700217.

[21] A.E. Ostfeld, A.M. Gaikwad, Y. Khan, A.C. Arias, High-performance flexible energy storage and harvesting system for wearable electronics, Sci. Rep. 6 (2016) 26122, https://doi.org/10.1038/srep26122.

[22] A.E. Ostfeld, I. Deckman, A.M. Gaikwad, C.M. Lochner, A.C. Arias, Screen printed passive components for flexible power electronics, Sci. Rep. 5 (2015) 15959, https://doi.org/10.1038/srep15959.

[23] Y. Khan, A. Thielens, S. Muin, J. Ting, C. Baumbauer, A.C. Arias, A new frontier of printed electronics: flexible hybrid electronic, Adv. Mater. 32 (2020) 1905279, https://doi.org/10.1002/adma.201905279.

[24] N.-B. Cho, T.-H. Lim, Y.-M. Jeon, M.-S. Gong, Humidity sensors fabricated with photo-curable electrolyte inks using an ink-jet printing technique and their properties, Sens. Actuators B Chem. 130 (2) (2008) 594–598, https://doi.org/10.1016/j.snb.2007.10.025.

[25] Y. Cheng, Y. Ma, L. Li, M. Zhu, Y. Yue, W. Liu, L. Wang, S. Jia, C. Li, T. Qi, J. Wang, Y. Gao, Bioinspired microspines for a high-performance spray $Ti_3C_2T_x$ MXene-based piezoresistive sensor, ACS Nano 14 (2) (2020) 2145–2155, https://doi.org/10.1021/acsnano.9b0895210.1021/acsnano.9b08952.s00110.1021/acsnano.9b08952.s00210.1021/acsnano.9b08952.s00310.1021/acsnano.9b08952.s004.

[26] T. Hasan, V. Scardaci, PingHeng Tan, A.G. Rozhin, W.I. Milne, A.C. Ferrari, Stabilization and "debundling" of single-wall carbon nanotube dispersions in N-Methyl-2-pyrrolidone (NMP) by Polyvinylpyrrolidone (PVP), J. Phys. Chem. C 111 (34) (2007) 12594–12602, https://doi.org/10.1021/jp0723012.

[27] M. Yang, K. Cao, L. Sui, Y. Qi, J. Zhu, A. Waas, E.M. Arruda, J. Kieffer, M. D. Thouless, N.A. Kotov, Dispersions of aramid nanofibers: a new nanoscale building block, ACS Nano 5 (9) (2011) 6945–6954, https://doi.org/10.1021/nn2014003.

[28] P. Hu, J. Lyu, C. Fu, W.-B. Gong, J. Liao, W. Lu, Y. Chen, X. Zhang, Multifunctional aramid nanofiber/carbon nanotube hybrid aerogel films, ACS Nano 14 (1) (2020) 688–697, https://doi.org/10.1021/acsnano.9b0745910.1021/acsnano.9b07459.s00110.1021/acsnano.9b07459.s00210.1021/acsnano.9b07459.s00310.1021/acsnano.9b07459.s004.

[29] Z. Ma, S. Kang, J. Ma, L. Shao, A. Wei, C. Liang, J. Gu, B. Yang, D. Dong, L. Wei, Z. Ji, High-performance and rapid-response electrical heaters based on ultraflexible, heat-resistant, and mechanically strong aramid/Ag nanowire nanocomposite papers, ACS Nano 13 (7) (2019) 7578–7590, https://doi.org/10.1021/acsnano.9b0043410.1021/acsnano.9b00434.s00110.1021/acsnano.9b00434.s00210.1021/acsnano.9b00434.s00310.1021/acsnano.9b00434.s004.

[30] J. Lyu, M.D. Hammig, L. Liu, L. Xu, H. Chi, C. Uher, T. Li, N.A. Kotov, Stretchable conductors by kirigami patterning of aramid-silver nanocomposites with zero conductance gradient, Appl. Phys. Lett. 111 (16) (2017) 161901, https://doi.org/10.1063/1.5001094.

[31] Y. Wan, Z. Qiu, Y. Hong, Y. Wang, J. Zhang, Q. Liu, Z. Wu, C.F. Guo, A highly sensitive flexible capacitive tactile sensor with sparse and high-aspect-ratio microstructures, Adv. Electron. Mater. 4 (4) (2018) 1700586, https://doi.org/10.1002/aelm.v4.410.1002/aelm.201700586.

[32] S.R.A. Ruth, V.R. Feig, H. Tran, Z. Bao, Microengineering pressure sensor active layers for improved performance, Adv. Funct. Mater. 30 (39) (2020) 2003491, https://doi.org/10.1002/adfm.v30.3910.1002/adfm.202003491.

[33] S.C.B. Mannsfeld, B.-K. Tee, R.M. Stoltenberg, C.-H. Chen, S. Barman, B.V.O. Muir, A.N. Sokolov, C. Reese, Z. Bao, Highly sensitive flexible pressure sensors with microstructured rubber dielectric layers, Nat. Mater. 9 (10) (2010) 859–864, https://doi.org/10.1038/nmat2834.

[34] J. Jia, G. Huang, J. Deng, K. Pan, Skin-inspired flexible and high-sensitivity pressure sensors based on rGO films with continuous-gradient wrinkles, Nanoscale 11 (10) (2019) 4258–4266, https://doi.org/10.1039/C8NR08503J.

[35] Y. Gao, C. Lu, Y.u. Guohui, J. Sha, J. Tan, F. Xuan, Laser micro-structured pressure sensor with modulated sensitivity for electronic skins, Nanotechnology 30 (32) (2019) 325502, https://doi.org/10.1088/1361-6528/ab1a86.

[36] Z. Dai, L. Liu, Z. Zhang, Strain engineering of 2D materials: issues and opportunities at the interface, Adv. Mater. 31 (45) (2019) 1805417, https://doi.org/10.1002/adma.v31.4510.1002/adma.201805417.

[37] S.R.A. Ruth, L. Beker, H. Tran, V.R. Feig, N. Matsuhisa, Z. Bao, Rational design of capacitive pressure sensors based on pyramidal microstructures for specialized monitoring of biosignals, Adv. Funct. Mater. 30 (29) (2020) 1903100, https://doi.org/10.1002/adfm.v30.2910.1002/adfm.201903100.

[38] Y. Wei, S. Chen, Y. Lin, Z. Yang, L. Liu, Cu-Ag core-shell nanowires for electronic skin with a petal molded microstructure, J. Mater. Chem. C 3 (37) (2015) 9594–9602, https://doi.org/10.1039/C5TC01723H.

[39] Y.u. Pang, K. Zhang, Z. Yang, S. Jiang, Z. Ju, Y. Li, X. Wang, D. Wang, M. Jian, Y. Zhang, R. Liang, H.e. Tian, Y.i. Yang, T.-L. Ren, Epidermis microstructure inspired graphene pressure sensor with random distributed spinosum for high sensitivity and large linearity, ACS Nano 12 (3) (2018) 2346–2354, https://doi.org/10.1021/acsnano.7b0761310.1021/acsnano.7b07613.s001.

[40] S. Wu, S. Yao, Y. Liu, X. Hu, H.H. Huang, Y. Zhu, Buckle-delamination-enabled stretchable silver nanowire conductors, ACS Appl. Mater. Interfaces 12 (37) (2020) 41696–41703, https://doi.org/10.1021/acsami.0c0977510.1021/acsami.0c09775.s001.

[41] L. Miao, J.i. Wan, Y.u. Song, H. Guo, H. Chen, X. Cheng, H. Zhang, Skin-inspired humidity and pressure sensor with a wrinkle-on-sponge structure, ACS Appl. Mater. Interfaces 11 (42) (2019) 39219–39227, https://doi.org/10.1021/acsami.9b1338310.1021/acsami.9b13383.s001.

[42] Q. Fu, Y.i. Chen, M. Sorieul, Wood-based flexible electronics, ACS Nano 14 (3) (2020) 3528–3538, https://doi.org/10.1021/acsnano.9b0981710.1021/acsnano.9b09817.s001.

[43] S. Cao, H. Pang, C. Zhao, S. Xuan, X. Gong, The CNT/PSt-EA/Kevlar composite with excellent ballistic performance, Compos. Part B-Eng. 185 (2020) 107793, https://doi.org/10.1016/j.compositesb:2020.107793.

[44] L. Penn, F. Milanovich, Raman-spectroscopy of Kevlar-49 fiber, Polymer 20 (1979) 31–36, https://doi.org/10.1016/0032-3861(79)90038-7.

[45] X. Chen, J.W. Hutchinson, Herringbone buckling patterns of compressed thin films on compliant substrates, J. Appl. Mech. 71 (2004) 597–603, https://doi.org/10.1115/1.1756141.

[46] R. HUANG, Kinetic wrinkling of an elastic film on a viscoelastic substrate, J. Mech. Phys. Solids 53 (1) (2005) 63–89, https://doi.org/10.1016/j.jmps.2004.06.007.

[47] Y.u. Cao, G. Zhang, Y. Zhang, M. Yue, Y. Chen, S. Cai, T. Xie, X. Feng, Direct fabrication of stretchable electronics on a polymer substrate with process-integrated programmable rigidity, Adv. Funct. Mater. 28 (50) (2018) 1804604, https://doi.org/10.1002/adfm.v28.5010.1002/adfm.201804604.

[48] J. Park, Y. Lee, J. Hong, M. Ha, Y.-D. Jung, H. Lim, S.Y. Kim, H. Ko, Giant tunneling piezoresistance of composite elastomers with interlocked microdome arrays for ultrasensitive and multimodal electronic skins, ACS Nano 8 (5) (2014) 4689–4697, https://doi.org/10.1021/nn500441k.

[49] A. Chortos, Z. Bao, Skin-inspired electronic devices, Mater. Today 17 (7) (2014) 321–331, https://doi.org/10.1016/j.mattod.2014.05.006.

[50] W.W. Nichols, Clinical measurement of arterial stiffness obtained from noninvasive pressure waveforms, Am. J. Hypertens. 18 (2005) 3S–10S, https://doi.org/10.1016/j.amjhyper.2004.10.009.

[51] N.A. Shirwany, M.-H. Zou, Arterial stiffness: a brief review, Acta Pharmacol. Sin. 31 (10) (2010) 1267–1276, https://doi.org/10.1038/aps.2010.123.

[52] J. Yang, J. Chen, Y. Su, Q. Jing, Z. Li, F. Yi, X. Wen, Z. Wang, Z.L. Wang, Eardrum-inspired active sensors for self-powered cardiovascular system characterization and throat-attached anti-interference voice recognition, Adv. Mater. 27 (8) (2015) 1316–1326, https://doi.org/10.1002/adma.201404794.

[53] I. O'Connor, H. Hayden, J.N. Coleman, Y.K. Gun'ko, High-strength, high-toughness composite fibers by swelling Kevlar in nanotube suspensions, Small 5 (4) (2009) 466–469, https://doi.org/10.1002/smll.v5:410.1002/smll.200801102.